Asymmetric Geodesic Distance Propagation for Active Contours

Da Chen[1, 4]
chenda@ceremade.dauphine.fr

Jack Spencer[2]
j.spencer@liverpool.ac.uk

Jean-Marie Mirebeau[3]
jean-marie.mirebeau@math.u-psud.fr

Ke Chen[2]
k.chen@liverpool.ac.uk

Laurent D. Cohen[1]
cohen@ceremade.dauphine.fr

[1] University Paris Dauphine, PSL Research University, CNRS, UMR 7534, CEREMADE, 75016 Paris, France

[2] Department of Mathematical Sciences, The University of Liverpool, UK

[3] Laboratoire de mathématiques d'Orsay, CNRS, Université Paris-Sud, Université Paris-Saclay, 91405 ORSAY, France

[4] Centre Hospitalier National d'Ophtalmologie des Quinze-Vingts, Paris, France

Abstract

The dual-front scheme is a powerful curve evolution tool for active contours and image segmentation, which has proven its capability in dealing with various segmentation tasks. In its basic formulation, a contour is represented by the interface of two adjacent Voronoi regions derived from the geodesic distance map which is the solution to an Eikonal equation. The original dual-front model [17] is based on isotropic metrics, and thus cannot take into account the asymmetric enhancements during curve evolution. In this paper, we propose a new asymmetric dual-front curve evolution model through an asymmetric Finsler geodesic metric, which is constructed in terms of the extended normal vector field of the current contour and the image data. The experimental results demonstrate the advantages of the proposed method in computational efficiency, robustness and accuracy when compared to the original isotropic dual-front model.

1 Introduction

Active contour models are a flexible segmentation tool that are able to benefit from the well-established energy minimization framework. Most of the existing active contour models aim to seek a family of closed curves to minimize a functional that is dependent on the region-based similarity measure and/or edge-based features such as image gradient. Since the original work of the snake model [14], the active contour approaches concentrate either on designing suitable energy functionals to address various segmentation problems in different situations, or on the improvement of the contour evolution schemes. Even though a large variety of energy functionals have been studied, the contour evolution tools have received little attention, which is the object of the method proposed in this paper.

Parametrized curves are a basic tool for active contour evolution where a contour is comprised of a set of ordered vertices or snaxels [7, 14, 19, 26]. It benefits from low computation

---

complexity leading to a series of successful applications in the task of tracking. However, the parametrized curve often suffers from the self-crossing problem in the course of the curve evolution, when dealing with the segmentation of an object with a complicated or noisy background [20]. Moreover, it is difficult for parametrized curves to handle the splitting or merging operation. In order to solve these problems, several curve evolution frameworks are exploited using either a continuous scheme [5, 21, 23] or a discrete scheme [10, 12].

For the continuous scheme, the level set method [21] has been broadly exploited for the active contour evolution [3, 27] in the past decades thanks to its solid mathematical guarantees. In the level set formulation, a closed (rectifiable) contour Γ can be reformulated as the zero-level set line of a signed Euclidean distance function $\phi : \Omega \to \mathbb{R}$ such that $\Gamma = \{x \in \Omega;\ \phi(x) = 0\}$. The level set scheme requires high computation complexity which prevents its practical applications in image segmentation. Many approaches have been devoted to improve the performance of the original level set formulation, such as the variational level set [28], the distance-preserved model [11, 16] and the Voronoi implicit interface model [23].

In contrast to the methods [11, 16, 23, 28] that use the *Euclidean* distance function to construct the level set lines, an alternative way is the dual-front scheme [17] which takes into account a geodesic distance map. During the evolution, a new contour can be recovered by detecting the common boundary of two adjacent Voronoi regions. The course of the geodesic distance propagation is similar to a wave front propagation. The distance computation is constrained by the narrowband region leading to an efficient implementation. One can also determine the thickness of the narrowband region providing the possibility of adequately finding the desired image boundary. One crucial component of the dual-front scheme is the geodesic metric. Basically, a suitable geodesic metric should be able to govern the fronts to travel fast in the homogeneous regions but slow in the vicinity of image edges. In [17], the authors used a class of isotropic metrics for the computation of the geodesic distances. This model cannot benefit from the geodesic asymmetric property because of its isotropic nature of the geodesic metrics used. In this paper, we propose a Finsler geodesic metric-based dual-front model for active contour evolution and image segmentation. The Finsler geodesic metric designed is derived from the image gradient information and the shape gradient of any adequate region-based active contour energy. Thus the proposed model can be taken as a general, efficient and robust curve evolution tool for image segmentation.

Paper Outline. In Section 2 we introduce the background on Voronoi Diagram computation in the sense of geodesic distance and the principle for the dual-front scheme. Section 3 presents the main contribution of this paper: how to construct a Finsler metric using the shape gradient of region-based energy and image gradients. In Section 4 we present the numerical implementation and the experimental results. Conclusions are presented in Section 5.

2   Voronoi Diagram Computation via Geodesic Distance

Let $\Omega \subset \mathbb{R}^2$ be an open bounded domain[1]. A closed contour Γ is a subset of Ω, which can be explicitly parametrized by a closed curve. Let $\mathbb{U}(\Gamma) \subset \Omega$ be a tubular neighbourhood of Γ with radius $\ell \in \mathbb{R}_0^+$. We denote by $\mathcal{R}(\Gamma) \subset \Omega$ the interior region of the contour Γ. The neighbourhood $\mathbb{U}(\Gamma)$ of Γ has two boundaries $\mathcal{C}_{\text{int}} \subset \mathcal{R}(\Gamma)$ and $\mathcal{C}_{\text{ext}} \subset \Omega \backslash \mathcal{R}(\Gamma)$.

Geodesic Distance Map and Voronoi Diagram. Let $\mathfrak{s}_k \subset \Omega$ be a family of source point sets which are indexed by $k \in \{1, 2, \cdots, n\}$. The geodesic distance value $\mathcal{U}_k(x)$ is defined as

---

[1]In this paper, we only consider the 2D case, i.e. $m = 2$, which can be straightforwardly extended to 3D.
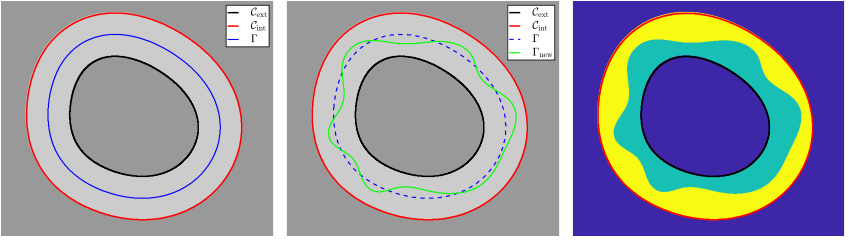
Figure 1: Dual-Front Scheme. On the left we show the contour Γ (blue curve), the interior boundary $\mathcal{C}_{\text{int}}$ (black curve) and the exterior boundary $\mathcal{C}_{\text{ext}}$ (red curve). In the middle we show the new contour Γ_{new} (green curve). On the right we show the Voronoi regions.

the minimal geodesic curve length between a point x and the set $\mathfrak{s}_k$ associated to a geodesic metric[2] $\mathcal{F} : \Omega \times \mathbb{R}^2 \to [0, \infty]$:

$$\mathcal{U}_k(x) = \inf_{y \in \mathfrak{s}_k} \left\{ \inf_{\gamma \in \text{Lips}(\Omega)} \left\{ \int_0^1 \mathcal{F}(\gamma(u), \gamma'(u)) du \right\}, \text{ s. t. } \gamma(0) = y, \ \gamma(1) = x \right\}, \quad (1)$$

where $\text{Lips}(\Omega)$ is the set of curves $\gamma : [0, 1] \to \Omega$ with Lipschitz continuity. The geodesic distance map $\mathcal{U}_k$ associated to a Finsler metric $\mathcal{F}$ is the unique viscosity solution to the Hamilton-Jacobi-Bellman (HJB) equation:

$$\mathcal{H}(x, \nabla \mathcal{U}_{\mathfrak{s}}(x)) = 1/2, \quad \forall x \in \Omega \backslash \mathfrak{s}, \quad (2)$$

with boundary condition $\mathcal{U}_{\mathfrak{s}}(x) = 0, \forall x \in \mathfrak{s}$, where $\mathcal{H} : \Omega \times \mathbb{R}^2 \to [0, \infty)$ is a Hamiltonian and $\nabla \mathcal{U}_{\mathfrak{s}}$ is the Euclidean gradient of $\mathcal{U}_{\mathfrak{s}}$. The Hamiltonian $\mathcal{H}$ can be expressed for any $x \in \Omega$ by

$$\mathcal{H}(x, \mathbf{u}) = \sup_{\mathbf{v} \in \mathbb{R}^2} \left\{ \langle \mathbf{u}, \mathbf{v} \rangle - \frac{1}{2} \mathcal{F}^2(x, \mathbf{v}) \right\}.$$

The Voronoi regions are defined in terms of the geodesic distance maps $\mathcal{U}_k$ by

$$\mathcal{V}_k = \{x \in \Omega; \mathcal{U}_k(x) = \mathcal{U}_*(x)\}, \quad \text{where} \quad \mathcal{U}_*(x) = \min_{1 \leq k \leq n} \mathcal{U}_k(x). \quad (3)$$

We use the Hamiltonian fast marching method[3] [18] which is based on Voronoi's first reduction technique as the numerical solver for the HJB equation (2). This is a generalization of the original fast marching method [24]. It can efficiently and accurately handle a variety of anisotropic and asymmetric Finsler metrics, such as $\mathcal{F}$ in Eq. (4), in addition to classical isotropic Riemannian metrics. The Hamiltonian fast marching is an efficient numerical solver with a computational time complexity $\mathcal{O}(m^2 N \log N)$, where m denotes the dimension of the domain and N is the total number of the points in the discretized domain. The computation of Voronoi regions can be done during the fast marching fronts propagation [6, 22].

Dual-Front Scheme. The dual-front model [17] proposed by Li and Yezzi uses the Voronoi diagram for the curve evolution scheme (see Fig. 1). Denoting by $\Gamma \subset \Omega$ a given closed contour, the objective for the dual-front model is to seek the next evolutional contour Γ_{new}. Based on the notations at the beginning of this section, we can compute the geodesic distance

---

[2]It is a convex and 1-homogeneous function on its second argument.
[3]The C++ codes can be downloaded from https://github.com/Mirebeau/HamiltonFastMarching.

maps $\mathcal{U}_{\text{int}}$ and $\mathcal{U}_{\text{ext}}$ by taking the boundaries $\mathcal{C}_{\text{int}}$ and $\mathcal{C}_{\text{ext}}$ as the respective source point sets. Note that the distance maps $\mathcal{U}_{\text{int}}$ and $\mathcal{U}_{\text{ext}}$ are estimated only within the neighbourhood $\mathbb{U}(\Gamma)$ for the sake of computational efficiency. Thus one can identify the Voronoi regions $\mathcal{V}_{\text{int}}$ and $\mathcal{V}_{\text{ext}}$ by Eq. (3). Then the new contour Γ_{new} is set as the common boundary of $\mathcal{V}_{\text{int}}$ and $\mathcal{V}_{\text{ext}}$. In the sense of curve evolution, one can construct a neighbourhood for the new contour Γ_{new} and repeat the procedure described above till the contour Γ_{new} converges to the desired object boundary. For this scheme, each geodesic distance map corresponds to an individual geodesic metric.

One crucial point for the dual-front model is the geodesic metrics $\mathcal{F}_{\text{int}}$ and $\mathcal{F}_{\text{ext}}$ that are used to estimate the distance maps $\mathcal{U}_{\text{int}}$ and $\mathcal{U}_{\text{ext}}$. The geodesic metrics in [17] are derived from the region-based similarity measure and image edge appearance features. However, these metrics used in [17] are only an isotropic case which is independent of the front directions. By these isotropic metrics, the fronts propagation might be terminated before finding the expected object boundaries. We generalize the isotropic dual-front model [17] by taking into account the shape gradient of any region-based active contour energy to build an anisotropic and asymmetric Finsler metric. In this case, the extended dual-front model can be a general tool for active contour models.

3   Finsler Metrics for Dual-Front Active Contours

We denote by $\langle \cdot, \cdot \rangle$ the Euclidean scalar product on $\mathbb{R}^2$, by S_2^+ the set of symmetric positive definite matrices, and by $\|\mathbf{u}\|_M = \sqrt{\langle \mathbf{u}, M\mathbf{u} \rangle}$ the anisotropic norm associated with a symmetric matrix $M \in S_2^+$. We consider an asymmetric Finsler metric $\mathcal{F}$ with a form

$$\mathcal{F}^2(x, \mathbf{u}) = \|\mathbf{u}\|^2_{\mathcal{M}(x)} + \langle \mathbf{u}, \omega(x) \rangle^2_-, \quad \langle \mathbf{u}, \mathbf{v} \rangle_- = \max\{-\langle \mathbf{u}, \mathbf{v} \rangle, 0\}, \quad (4)$$

where $\mathcal{M} : \Omega \to S_2^+$ is a definite positive symmetric tensor field and $\omega : \Omega \to \mathbb{R}^2$ is a vector field. The Finsler metric[4] $\mathcal{F}$ formulated in Eq. (4) is said to be asymmetric with respect to its second argument by the fact that $\exists x \in \Omega$ and $\exists \mathbf{u} \in \mathbb{R}^2$ such that $\mathcal{F}(x, \mathbf{u}) \neq \mathcal{F}(x, -\mathbf{u})$. The asymmetry property of the Finsler metric $\mathcal{F}$ is from its second term associated to the vector field ω. Obviously, when the vector field ω satisfies $\omega \equiv \mathbf{0}$, the metric $\mathcal{F}$ gets to a symmetric Riemannian case.

The crucial point for the Finsler metric $\mathcal{F}$ is the computation of $\mathcal{M}$ and ω. Suppose that a feature vector field $\mathbf{p} : \Omega \to \mathbb{R}^2$ with $\|\mathbf{p}\| \equiv 1$ is given. The computation of $\mathbf{p}$ are detailed in Section 3.1. Now we give the construction method for the tensor field $\mathcal{M}$ and the vector field ω through the feature vector field $\mathbf{p}$ and three scalar functions $\varsigma, \mu, \lambda : \Omega \to \mathbb{R}^+$ by

$$\mathcal{M}(x) = \varsigma^2(x)\mathbf{p}(x)\mathbf{p}(x)^T + \mu^2(x)\mathbf{p}_\perp(x)\mathbf{p}_\perp(x)^T, \quad s.t. \quad \varsigma(x) \leq \mu(x), \quad (5)$$

$$\omega(x) = \sqrt{\max\{0, \lambda^2(x)\mu^2(x) - \varsigma^2(x)\}} \ \mathbf{p}(x). \quad (6)$$

The vector $\mathbf{p}_\perp(x)$ is orthogonal to $\mathbf{p}(x)$ and $\varsigma^2(x), \mu^2(x)$ are the eigenvalues of $\mathcal{M}(x)$ with respect to eigenvectors $\mathbf{p}(x)$ and $\mathbf{p}_\perp(x)$. The metric $\mathcal{F}(x, \cdot)$ is asymmetric at point x in the case $\lambda(x)\mu(x) > \varsigma(x)$. For each point x, the speed of the fronts along the directions $\mathbf{p}(x)$, $\mathbf{p}_\perp(x)$, and $-\mathbf{p}(x)$ are respectively $\varsigma(x)$, $\mu(x)$ and $\lambda(x)\mu(x)$. With respect to the dual-front

---

[4]Note that a form similar to the one of (4) was used by the authors of [9] to build an orientation-lifted Finsler metric for curvature-penalized geodesic computation, while here we use this form for image segmentation.
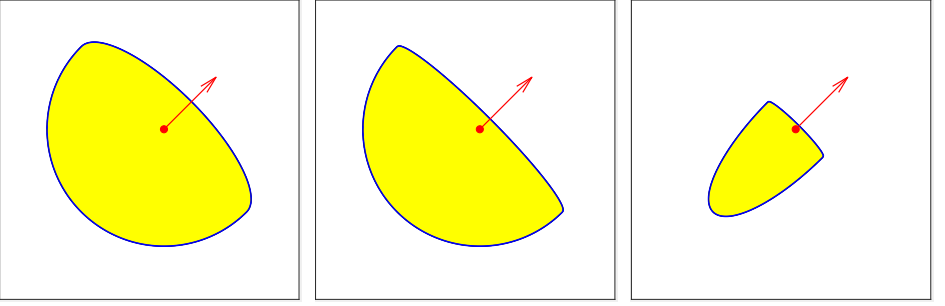
Figure 2: Control sets with different values of $\mu(x)$ and $\lambda(x)$ and with $\varsigma \equiv 1$. **Left**: $\mu(x) = 1$ and $\lambda(x) = 3$. **Middle**: $\mu(x) = 1$ and $\lambda(x) = 8$. **Right**: $\mu(x) = 3$ and $\lambda(x)=8$. The red dots are the origins of the control sets $\mathcal{B}(x)$. The arrow indicates the vector $\mathbf{p}(x)$.
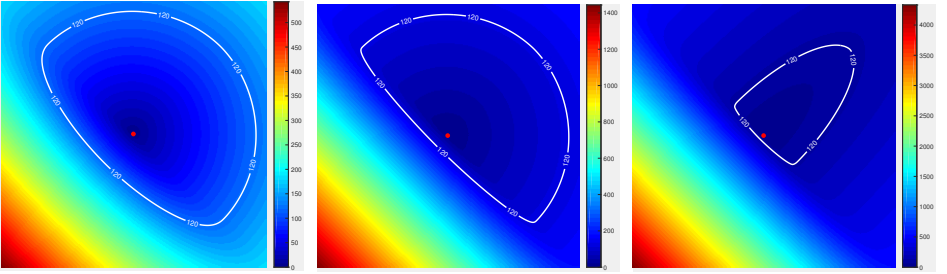

Figure 3: Geodesic distance maps associated to the Finsler metrics for which the control sets at each point are shown in the corresponding columns of Fig. 2.

scheme [□], the segmentation is determined in terms of the respective Voronoi regions. By adequately designing the feature vector field $\mathbf{p}$ and the functions ς, μ and λ, we can control the velocities for the fronts expanding from the exterior and interior contours, leading to a suitable Voronoi region partitioning. The computation for the functions ς, μ, λ and the feature vector field $\mathbf{p}$ are described in Section 3.1.

Here we show some geometric properties of the metric $\mathcal{F}$ formulated in Eq. (4) with respect to different $\mathcal{M}$ and ω. A basic tool for characterizing the metric $\mathcal{F}$ is its control set $\mathcal{B}$ which is a collection of unit balls which can be expressed as $\mathcal{B}(x) = \{\mathbf{u} \in \mathbb{R}^2; \mathcal{F}(x, \mathbf{u}) \leq 1\}$. In Fig. 2, we illustrate the control sets $\mathcal{B}(x)$ associated to three Finsler metrics $\mathcal{F}$ at a point x. We fix that $\varsigma \equiv 1$ and $\mathbf{p} \equiv (\cos(\pi/4), \sin(\pi/4))^T$. In columns 1 to 3 of Fig. 2, we use different values of μ and λ to construct these Finsler metrics. Note that for the sake of simplicity, in this experiment we set μ and λ to be constant functions. The geodesic distance maps associated to the Finsler metrics, which are used in the corresponding columns of Fig 2 for control set demonstration, are shown in Fig. 3.

3.1 Finsler Metric Construction

In this section, we use the region-based similarity measure to compute the Finsler metrics for dual-front scheme. According to the dual-front scheme (see [□] or Section 2), for each tubular neighbourhood boundary (either $\mathcal{C}_{\text{int}}$ or $\mathcal{C}_{\text{ext}}$) we need to design a Finsler geodesic

metric (denoted by $\mathcal{F}_{\text{int}}$ and $\mathcal{F}_{\text{ext}}$ respectively), in order to compute the associated Voronoi diagram. We define an extended normal vector field $\mathfrak{N}$:

Definition 1. *Consider a closed contour $\partial \hbar$ which is the boundary of a shape $\hbar$ and let $\mathcal{N}_{\partial \hbar} : \partial \hbar \to \mathbb{R}^2$ be its unit normal. We define a vector field $\mathfrak{N}_\hbar : \Omega \to \mathbb{R}^2$ being such that*

$$\mathfrak{N}_\hbar(x) = \mathcal{N}_{\partial \hbar}(x), \ \forall x \in \partial \hbar, \quad \text{and} \quad \mathfrak{N}_\hbar(x) = \nabla d_{\partial \hbar}(x), \ \forall x \in \mathbb{U}(\partial \hbar) \backslash \partial \hbar, \tag{7}$$

where $d_{\partial \hbar} : \mathbb{U}(\partial \hbar) \to \mathbb{R}_0^+$ is a Euclidean distance map associated to the contour $\partial \hbar$, i.e., $d_{\partial \hbar}(x) = \min_{y \in \mathbb{U}(\partial \hbar)} \|x - y\|$. In this case, the vector field $\mathfrak{N}_\hbar$ gets to be an extension of $\mathcal{N}_{\partial \hbar}$.

We suppose that a shape $\hbar$ is an arbitrary measurable subset of the domain Ω with a rectifiable boundary $\partial \hbar$. For a region-based functional $E_\hbar$ associated to a fixed shape $\hbar$, we denote its shape gradient [1] at the shape $\hbar$ by $\psi_\hbar$, which can be obtained via the Gâteaux derivative of the functional $E_\hbar$ along an admissible perturbation. For simplicity, we define a variant shape gradient function $\mathfrak{C}_\hbar : \Omega \to \mathbb{R}$ as

$$\mathfrak{C}_\hbar(x) = -\psi_\hbar(x), \ \forall x \in \hbar, \quad \text{and} \quad \mathfrak{C}_\hbar(x) = \psi_\hbar(x), \ \forall x \in \Omega \backslash \hbar. \tag{8}$$

Through the function $\mathfrak{C}_\hbar$, we divide the tubular region $\mathbb{U}(\partial \hbar)$ into four subregions:

$$\mathbb{U}_{\text{int}}^+ := \{x \in \hbar, \mathfrak{C}(x) \geq 0\}, \qquad \mathbb{U}_{\text{int}}^- := \{x \in \hbar, \mathfrak{C}(x) < 0\}, \tag{9}$$
$$\mathbb{U}_{\text{ext}}^+ := \{x \in \Omega \backslash \hbar, \mathfrak{C}(x) \geq 0\}, \quad \mathbb{U}_{\text{ext}}^- := \{x \in \Omega \backslash \hbar, \mathfrak{C}(x) < 0\}. \tag{10}$$

Recall that the fronts expanding from the internal and external tube boundaries $\mathcal{C}_{\text{int}}$ and $\mathcal{C}_{\text{ext}}$ depend on the Finsler metrics $\mathcal{F}_{\text{int}}$ and $\mathcal{F}_{\text{ext}}$, respectively. Let $\hbar^*$ be a shape obtained in a deformable manner from the initial shape $\hbar$. If $\hbar^*$ is a minimizer for the region-based energy $E_\hbar$, its boundary $\partial \hbar^*$ should be a subset of the zero-crossing point set of $\psi_\hbar$. Our goal is to seek a shape $\hbar^* \subset \Omega$ such that in some tubular neighbourhood $\mathbb{U}(\partial \hbar^*)$ of the shape boundary $\partial \hbar^*$, the inequality $\mathfrak{C}_\hbar(x) \geq 0$ can hold. One possible solution is to make the front which expands from the internal tube boundary travel slower in the region $\mathbb{U}_{\text{int}}^-$ than the front from the external tube boundary $\mathcal{C}_{\text{ext}}$. For this purpose, we can design the Finsler metrics $\mathcal{F}_{\text{int}}$ and $\mathcal{F}_{\text{ext}}$ such that $\mathcal{F}_{\text{int}}(x, \mathfrak{N}(x)) > \mathcal{F}_{\text{ext}}(x, -\mathfrak{N}(x)), \ \forall x \in \mathbb{U}_{\text{int}}^-$. Alternatively, for each point $x \in \mathbb{U}_{\text{ext}}^-$, the Finsler metrics should satisfy $\mathcal{F}_{\text{ext}}(x, \mathfrak{N}(x)) > \mathcal{F}_{\text{int}}(x, -\mathfrak{N}(x))$ in order to expand the front associated to $\mathcal{F}_{\text{ext}}$ slower than the front from the internal tube boundary.

Computation of the eigenvalue functions ς and μ. The eigenvalue functions ς and μ should be computed individually for each of the Finsler metrics $\mathcal{F}_{\text{int}}$ and $\mathcal{F}_{\text{ext}}$. The fronts from the tube boundaries $\mathcal{C}_{\text{int}}$ and $\mathcal{C}_{\text{ext}}$ are expected to meet at the zero-crossing points of the shape gradient $\psi_\hbar$. For this purpose, we set the eigenvalue functions for the metric $\mathcal{F}_{\text{ext}}$ as

$$\varsigma_{\text{ext}}(x) = \exp(\beta \tau(x)) \exp(-\alpha \psi_\hbar(x)), \quad \mu_{\text{ext}} \equiv \varsigma_{\text{ext}}, \tag{11}$$

and the metric $\mathcal{F}_{\text{int}}$ as

$$\varsigma_{\text{int}}(x) = \exp(\beta \tau(x)) \exp(\alpha \psi_\hbar(x)), \quad \mu_{\text{int}} \equiv \varsigma_{\text{int}}, \tag{12}$$

where α and β are positive constants. The function $\tau : \Omega \to [0, 1]$ is a normalized edge appearance indicating function. For a vector-valued image $\mathbf{I} = (I_1, I_2, I_3) : \Omega \to \mathbb{R}^3$ in the RGB colour space, the edge appearance function τ can be computed using the Gaussian-smoothed colour gradient $\nabla \mathbf{I}_\sigma(x) = (\nabla G_\sigma * \mathbf{I})(x)$, where G_σ is a Gaussian kernel with variance σ.
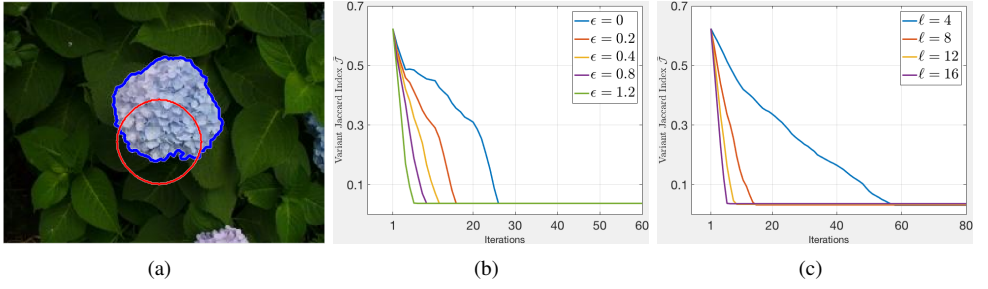
Figure 4: Convergence rates for different values of ε and ℓ. **(a)** The initial contour (red curve) and the segmentation (blue curve). **(b)** The curves of $\bar{\mathcal{J}}$ for different values of ε during the shape evolution. **(c)** The curves of $\bar{\mathcal{J}}$ for different values of ℓ during the shape evolution.

Note that $\nabla \mathbf{I}_\sigma(x)$ is a 2×3 Jacobian matrix. The edge appearance function τ of the image $\mathbf{I}$ can be computed via the Frobenius norm of the Jacobian matrix $\nabla \mathbf{I}_\sigma(x)$ such that

$$\tau(x) = \frac{\tau_0(x)}{\|\tau_0\|_\infty}, \quad \text{where } \tau_0(x) = \sqrt{\sum_{i=1}^{3} \|(\nabla G_\sigma * I_i)(x)\|^2}.$$

Computation of the asymmetric penalty λ and the feature vector field p. The asymmetric penalty function λ can be computed in terms of the function $\mathfrak{C}_\hbar$ such that

$$\lambda(x) = \exp(-\varepsilon \, \mathfrak{C}_\hbar(x)), \tag{13}$$

where $\varepsilon \in \mathbb{R}^+$ is a positive constant. For each point $x \in \mathbb{U}_{\text{int}}^+ \cup \mathbb{U}_{\text{ext}}^+ = \{x \in \mathbb{U}; \mathfrak{C}(x) \geq 0\}$, we have $\lambda(x) \leq 1$ leading to $\omega(x) = \mathbf{0}$ (see Eq. (6)). In this case, the metrics $\mathcal{F}_{\text{int}}$ and $\mathcal{F}_{\text{ext}}$ get to be the isotropic metrics. Thus, the metrics $\mathcal{F}_{\text{int}}(x, \cdot)$ and $\mathcal{F}_{\text{ext}}(x, \cdot)$ are independent of the vectors $\mathbf{p}(x)$ for the points x such that $\mathfrak{C}(x) \geq 0$. In order to follow the criteria $\mathcal{F}_{\text{int}}(x, \mathfrak{N}(x)) > \mathcal{F}_{\text{ext}}(x, -\mathfrak{N}(x))$, $\forall x \in \mathbb{U}_{\text{int}}^-$ and $\mathcal{F}_{\text{ext}}(x, \mathfrak{N}(x)) > \mathcal{F}_{\text{int}}(x, -\mathfrak{N}(x))$, $\forall x \in \mathbb{U}_{\text{ext}}^-$, we construct the feature vector field $\mathbf{p}$ by

$$\mathbf{p}(x) = \mathfrak{N}_\hbar(x). \tag{14}$$

In the numerical experiments, we further set $\lambda(x) = 1$, $\forall x \in \partial \hbar$. For the points $x \in \mathbb{U}_{\text{int}}^- \cup \mathbb{U}_{\text{ext}}^- = \{x \in \mathbb{U}; \mathfrak{C}_\hbar(x) < 0\}$, the Finsler metrics $\mathcal{F}_{\text{int}}$ and $\mathcal{F}_{\text{ext}}$ are strongly asymmetric. It can help the dual-front propagation scheme to reduce the risk of the front shortcut problem, which will be illustrated in the following experiments.

Remark 1. The class of asymmetric Finsler metrics as defined in Eq. (4), allows us to independently set the front propagation speed in one direction and in the opposite direction, such as $\mathfrak{N}(x)$ and $-\mathfrak{N}(x)$ at a point x in the tubular neighbourhood. Therefore, the conditions could in principle be achieved using a single metric $\mathcal{F} = \mathcal{F}_{\text{int}} = \mathcal{F}_{\text{ext}}$ with $\alpha = 0$, in contrast with previous works [17]. This potential simplification was one of our initial motivations for the study of active contours based on asymmetric geodesic distances. However, in the end, we found that the best efficiency was achieved by combining the advantages of both (i) asymmetric metrics, and (ii) distinct metrics for the two fronts.
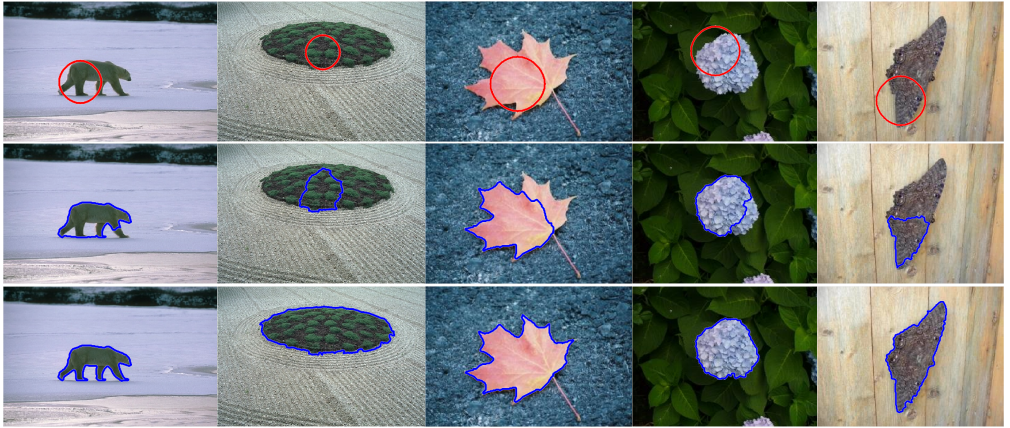
Figure 5: Comparative results of the dual-front method with isotropic and Finsler metrics. **Row 1** Initial contours indicated by red curves. **Row 2** Segmentation from isotropic dual-front scheme. **Row 3** Segmentation from the proposed Finsler dual-front scheme.

4   Experimental Results

In this section we illustrate the results of the dual-front scheme with the proposed asymmetric Finsler metric, involving the study of the proposed model itself and the comparisons with the original dual-front scheme [□].

Chan-Vese Active Contour Energy. The Chan-Vese model [□] invokes two vectors $\eta^{\text{int}} = \{\eta_i^{\text{int}}\}_{1 \leq i \leq 3}$ and $\eta^{\text{ext}} = \{\eta_i^{\text{ext}}\}_{1 \leq i \leq 3}$, to approximate the intensities inside and outside the contour Γ of a vector-valued image $\mathbf{I}$

$$E_\hbar(\Gamma) = \int_{\mathcal{R}(\Gamma)} \sum_i (I_i(x) - \eta_i^{\text{int}})^2 dx + \int_{\Omega \setminus \mathcal{R}(\Gamma)} \sum_i (I_i(x) - \eta_i^{\text{ext}})^2 dx,$$

where η_i^{int} and η_i^{ext} are the mean intensity values inside and outside the contour $\partial \hbar$ of the ith image channel I_i. The shape gradient $\psi_\hbar$ for the Chan-Vese energy $E_\hbar$ can be expressed by

$$\psi_\hbar(x) = \sum_i \left((I_i(x) - \eta_i^{\text{int}})^2 - (I_i(x) - \eta_i^{\text{ext}})^2 \right). \tag{15}$$

In the following experiments, we normalize the shape gradient $\psi_\hbar$ to the range $[-1, 1]$.
Influence of Different Values of the Parameters. We show the influences from the parameters to be set up in our model. First, the parameter ε in Eq. (13) dominates the asymmetric penalty for the Finsler metrics $\mathcal{F}_{\text{ext}}$ and $\mathcal{F}_{\text{int}}$. Secondly, the parameters α and β in Eqs. (11) and (12) control the influence from the image data. Finally, the value of ℓ controls the width of the tubular neighbourhood. In the following, we show how ε and ℓ affect the convergence rate of the Finsler dual-front model. We set the discretization scale to be 1.

In Fig. 4, the parameters α and β are set to 0.5 and 10, respectively. We consider different values of ε and ℓ to show how the convergence rates of the dual-front scheme are affected by the asymmetry penalty and the tubular neighbourhood width. For this purpose, we compute a variant Jaccard index $\bar{\mathcal{J}}(S, G) = 1 - \mathcal{J}(S, G)$ between the current shape S and the groundtruth

G, where $\mathcal{J}(S,G) = |S \cap G|/|S \cup G|$ with $|S|$ and $|G|$ the areas of S and G. In Fig. 4a, we show the original image with initial contour (red curve) and the final segmentation (blue curve). In Fig. 4b, we plot the values of $\bar{\mathcal{J}}$ for the proposed Finsler dual-front method with values of ε being set to 0, 0.2, 0.4, 0.8, and 1.2, respectively. One can point out that a large value of ε which implies strong asymmetry leads to a fast convergence rate. In Fig. 4c, we fix $\beta = 10$ and $\varepsilon = 1$. The convergence rate associated with different values of tubular neighbourhood radii ℓ is tested by setting $\ell = 4, 8, 12$ and 16 respectively. One can see that a sufficiently large ℓ could speed up the convergence of the dual-front scheme.

In Fig. 5, we show the comparative results on the isotropic dual-front model [17] and the proposed Finsler dual-front model. In the first row of Fig. 5, we show the original images with initial contours. The second and the third rows are the results derived from the isotropic and Finsler dual-front models, respectively. For the sake of fair comparison, we use the same values of α, β and ℓ for both models. More specifically, we set $\alpha = 0.3$, $\beta = 10$ and $\ell = 16$. The dual-front propagation will be terminated when the two contours of the adjacent iterations are close enough. One can point out that the final segmentation contours from the isotropic model are trapped to the false positions, while the proposed Finsler dual-front model can find the expected segmentation thanks to the asymmetric penalty.

In Table. 1, we show the quantitive comparisons between the isotropic and Finsler dual-front models on the images shown in Fig. 5. For each image, we run the dual-front models with different metrics for 30 times and we compute the statistical information including the maximum (Max.), minimum (Min.), average (Avg.) and standard derivation (Std.) values of the Jaccard index $\mathcal{J}$ for these 30 experiments. In each dual-front running, the initial contour is set as a circle with radius 40, the centre point of which is chosen by randomly sampling a point that is inside the target. We set $\alpha = 0.3$, $\beta = 10$ and $\ell = 16$ for both the isotropic and Finsler dual-front models. Specifically, we set $\varepsilon = 1$ for the dual-front model with the proposed Finsler metrics. From Table. 1, one can see that through the 30 segmentation experiments on each image, the Finsler dual-front model achieves higher Avg. and Max. Jaccard index values than the isotropic model. Meanwhile, the standard derivation of $\mathcal{J}$ from the Finsler dual-front model is lower than the isotropic model. This implies the proposed Finsler dual-front model is more accurate and more robust to initialization compared to the isotropic case [17], even if the parameter α is set to a small value.

Note that through the comparative experiments we make use of a small value of α in order to demonstrate the advantages of using the asymmetric Finsler metrics for dual-front propagation. For a small value of α, in each iteration, it is difficult for the isotropic dual-front model to shift the interface of the two fronts toward the desired object boundaries. While for the proposed Finsler case, the asymmetric penalty leads to a fast fronts motion by assigning a large distance values to the front points for which the advancing directions are unexpected.

Remark 2. In the context of image segmentation, the minimal path-based approaches, such as the region-based Eikonal active contours method [7] and the Finsler ealstica method [8] represent the object boundaries via a set of geodesic curves, which cannot be straightforwardly extended to surface evolution. In contrast, the dual-front scheme can be naturally extended to 3D volume segmentation since the segmentation scheme is carried out by the fronts of the geodesic distances instead of the geodesics themselves.

Remark 3. In this paper, for the sake of simplicity, we only consider the classic piecewise constant active contour energy [4] to construct the Finsler geodesic metrics. However, the proposed model can be adapted to a broad variety of active contour energies to deal with more complicated segmentation situations, for example the pairwise similarity-based active contours models [2, 13, 25].

Table 1: Quantitative results of the isotropic and Finsler models on the images in Fig. 5.

IMAGES		Col. 1	Col. 2	Col. 3	Col. 4	Col. 5
Isotropic Model [15]	Avg.	0.794	0.204	0.769	0.746	0.584
	Max.	0.886	0.38	0.946	0.965	0.813
	Min.	0.363	0.084	0.289	0.368	0.189
	Std.	0.147	0.074	0.209	0.219	0.169
Proposed Finsler Model	Avg.	0.946	0.971	0.945	0.965	0.958
	Max.	0.946	0.971	0.946	0.965	0.959
	Min.	0.946	0.969	0.945	0.965	0.957
	Std.	≈ 0	≈ 0	≈ 0	≈ 0	≈ 0

5 Conclusion

In this paper, we propose a new Finsler dual-front model for image segmentation. We extend the isotropic dual-front model [17] to the generally asymmetric and anisotropic Finsler case. A crucial contribution is the construction method of the Finsler geodesic metric with an asymmetric quadratic form. This Finsler metric is able to take advantages from the shape gradient of a region-based energy and the image gradient features. Compared to the isotropic case, the proposed Finsler dual-front scheme can reduce the risk of detecting spurious contours. Thus the proposed Finsler dual-front model is able to obtain more accurate and more robust segmentations. In future, we will extend this work to the applications of 2D multi-region segmentation and 3D volume segmentation, integrating with the edge anisotropy.

Acknowledgement

References

[1] G. Aubert, M. Barlaud, O. Faugeras, and S. Jehan-Besson. Image segmentation using active contours: Calculus of variations or shape gradients? *SIAM J. Appl. Math.*, 63 (6):2128–2154, 2003.

[2] L. Bertelli, B. Sumengen, BS Manjunath, and F. Gibou. A variational framework for multiregion pairwise-similarity-based image segmentation. *IEEE Trans. Pattern Anal. Mach. Intell.*, 30(8):1400–1414, 2008.

[3] V. Caselles, R. Kimmel, and G. Sapiro. Geodesic active contours. *Int. J. Comput. Vis.*, 22(1):61–79, 1997.

[4] T. F. Chan and L. A. Vese. Active contours without edges. *IEEE Trans. Image Process.*, 10(2):266–277, 2001.

[5] T. F. Chan, S. Esedoglu, and M. Nikolova. Algorithms for finding global minimizers of image segmentation and denoising models. *SIAM J. Appl. Math.*, 66(5):1632–1648, 2006.

[6] D. Chen and L. D. Cohen. Fast asymmetric fronts propagation for image segmentation. *J. Math. Imaging Vis.*, 60(6):766–783, 2018.

[7] D. Chen, J.-M. Mirebeau, and L. D. Cohen. Finsler geodesics evolution model for region based active contours. In *Proc. BMVC*, 2016.

[8] D. Chen, J.-M. Mirebeau, and L. D. Cohen. Global minimum for a Finsler elastica minimal path approach. *Int. J. Comput. Vis.*, 122(3):458–483, 2017.

[9] R. Duits, S. P. L. Meesters, J.-M. Mirebeau, and J. M. Portegies. Optimal paths for variants of the 2D and 3D Reeds–Shepp car with applications in image analysis. *J. Math. Imag. Vis.*, 60(6):816–848, 2018.

[10] N. Y. El-Zehiry and L. Grady. Combinatorial optimization of the discretized multiphase Mumford–Shah functional. *Int. J. Comput. Vis.*, 104(3):270–285, 2013.

[11] V. Estellers, D. Zosso, R. Lai, S. Osher, J.-P. Thiran, and X. Bresson. Efficient algorithm for level set method preserving distance function. *IEEE Trans. Image Process.*, 21(12):4722–4734, 2012.

[12] L. Grady and C. V. Alvino. The piecewise smooth Mumford–Shah functional on an arbitrary graph. *IEEE Trans. Image Process.*, 18(11):2547–2561, 2009.

[13] M. Jung, G. Peyré, and L. D. Cohen. Nonlocal active contours. *SIAM J. Imaging Sci.*, 5(3):1022–1054, 2012.

[14] M. Kass, A. Witkin, and D. Terzopoulos. Snakes: Active contour models. *Int. J. Comput. Vis.*, 1(4):321–331, 1988.

[15] B. Li and S. T. Acton. Active contour external force using vector field convolution for image segmentation. *IEEE Trans. Image Process.*, 16(8):2096–2106, 2007.

[16] C. Li, C. Xu, C. Gui, and M. D. Fox. Distance regularized level set evolution and its application to image segmentation. *IEEE Trans. Image Process.*, 19(12):3243–3254, 2010.

[17] H. Li and A. Yezzi. Local or global minima: Flexible dual-front active contours. *IEEE Trans. Pattern Anal. Mach. Intell.*, 29(1), 2007.

[18] J.-M. Mirebeau. Anisotropic fast-marching on cartesian grids using voronoi's first reduction of quadratic forms. *https://hal.archives-ouvertes.fr/hal-01507334*, 2017.

[19] A. K. Mishra, P. W. Fieguth, and D. A. Clausi. Decoupled active contour (DAC) for boundary detection. *IEEE Trans. Pattern Anal. Mach. Intell.*, 33(2):310–324, 2011.

[20] A. Nakhmani and A. Tannenbaum. Self-crossing detection and location for parametric active contours. *IEEE Trans. Image Process.*, 21(7):3150–3156, 2012.

[21] S. Osher and J. A. Sethian. Fronts propagating with curvature-dependent speed: algorithms based on Hamilton-Jacobi formulations. *J. Comput. Phys.*, 79(1):12–49, 1988.

[22] G. Peyré, M. Péchaud, R. Keriven, and L. D. Cohen. Geodesic methods in computer vision and graphics. *Foundations and Trends® in Computer Graphics and Vision*, 5 (3–4):197–397, 2010.

[23] R. Saye and J. A. Sethian. Analysis and applications of the Voronoi implicit interface method. *J. Comput. Phys.*, 231(18):6051–6085, 2012.

[24] J. A. Sethian. Fast marching methods. *SIAM Review*, 41(2):199–235, 1999.

[25] B. Sumengen and BS Manjunath. Graph partitioning active contours (GPAC) for image segmentation. *IEEE Trans. Pattern Anal. Mach. Intell.*, 28(4):509–521, 2006.

[26] C. Xu and J. L. Prince. Snakes, shapes, and gradient vector flow. *IEEE Trans. Image Process.*, 7(3):359–369, 1998.

[27] A. Yezzi, S. Kichenassamy, A. Kumar, P. Olver, and A. Tannenbaum. A geometric snake model for segmentation of medical imagery. *IEEE Trans. Med. Imaging*, 16(2): 199–209, 1997.

[28] H. Zhao, T. F. Chan, B. Merriman, and S. Osher. A variational level set approach to multiphase motion. *J. Comput. Phys.*, 127(1):179–195, 1996.